NJC

Accepted Manuscript

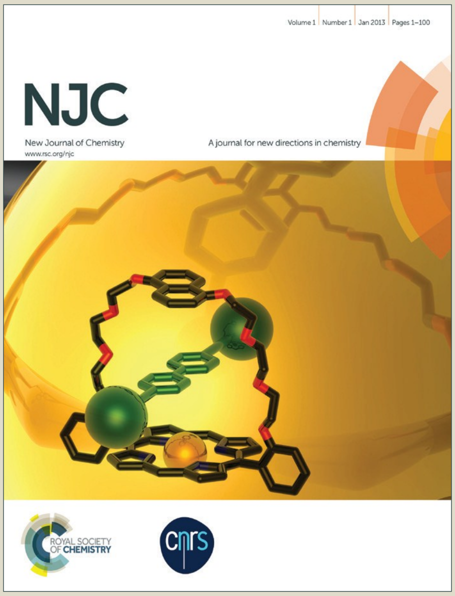

ROYAL SOCIETY OF CHEMISTRY

www.rsc.org/njc

NJC

ARTICLE

Electrodic Reduction of Core-Shell Ferrite Magnetic Nanoparticles

Received 00th Month 2016,
Accepted 00th Month 2016

DOI: 10.1039/x0xx00000x

www.rsc.org/njc

Cleber Lopes Filomeno,[a,c] Epitácio Pinto Marinho,[a] Renata Aquino,[a,b] Franciscarlos Gomes da Silva,[a,b] Emmanuelle Dubois,[c] Jerome Depeyrot,[a] and Alex Fabiano Cortez Campos,[a,b]

We present Square-Wave Voltammetry (SWV) and Controlled Potential Coulometry (bulk electrolysis) experiments performed on maghemite and ferrite nanoparticles of core-shell type $MFe_2O_4@\gamma\text{-}Fe_2O_3$ (where M = Mn^{2+}, Co^{2+}, Cu^{2+} or Zn^{2+}), dispersed in aqueous media. The potential position of iron (III) reduction peak identified in SWV measurements does not depend on the core chemical composition. No variations with size and polydispersity are detected. The shift of the reduction peak observed in coordinated configurations is related with iron oxidizing strength. The electrolysis performed at a controlled potential of NPs indicate that only a fraction of iron (III) is reduced. Using the individual net charge deduced from Controlled Potential Coulometry measurements, we determine the thickness of the surface shell, which is electrolyzed.

Introduction

Magnetic nanoparticles (NPs) and ferrofluids (FFs) are a class of materials broadly known due to their functional and relevant properties to sophisticated applications in biotechnological and biomedical fields.[1,2] In the case of hyperthermia applications, the use of NPs, such as mixed ferrites or core-shell ones, open the panorama to target the magneto-thermic properties to specific therapies.[3,4] In this context, aqueous FFs based on core-shell NPs rise as good precursors for this kind of applications, since it brings together magnetic, flow and colloidal properties.

Several studies have focused on the significant changes and new features on the magnetic properties of spinel ferrite NPs that emerge from the core-shell structure.[5-9] Recent investigations on exchange bias properties of core-shell $MnFe_2O_4@\gamma\text{-}Fe_2O_3$ [5] and $CoFe_2O_4@\gamma\text{-}Fe_2O_3$ [6] based FFs have demonstrated that the magnetic coupling between such soft or hard ferrite cores with the maghemite ($\gamma\text{-}Fe_2O_3$) shell can give a better understanding of the conversion of electromagnetic energy into heating efficiency in magnetic NP hyperthermia.[10-13] Also for $CoFe_2O_4@MnFe_2O_4$ NPs, a recent study has shown that due to the core-shell exchange-coupling, the specific loss power values (parameter which categorizes the NP suitable for hyperthermia) are larger than conventionally used iron-oxide nanoparticles, evidencing the relevance of this kind of systems for advanced nanotechnological applications.[14] Indeed, several NPs properties are influenced and directed related to the detailed structure and the core-shell composition. Previous investigations of the chemical composition and structure of core-shell $NiFe_2O_4@\gamma\text{-}Fe_2O_3$, $CuFe_2O_4@\gamma\text{-}Fe_2O_3$ and $ZnFe_2O_4@\gamma\text{-}Fe_2O_3$ NPs[7, 8] demonstrate that the heterogeneous composition of these particles seems to present no distortions in the crystalline spinel ferrite structures. Moreover, the shell thickness and the tunable core composition of NPs appear as very important parameters for the effective magnetization properties of these systems.

In parallel to the internal NPs structure and composition, the interface of particle/carrier solvent is an important point for the properties of core-shell based FFs systems, such as colloidal stability and interparticle interactions. The characteristics of NPs surface provide the ability to form well-dispersed systems, even in acidic, alkaline or neutral pH medium. In such a context, we have recently shown that electrochemical techniques are useful to study the acid-base equilibrium between particle surface and electrolytic free solution.[15] So simultaneous potentiometric and conductometric titrations, for aqueous FFs, have allowed us to determine the NP surface charge density. The results also reveal that the surface charge depends on the particle sizes; the surface acidity is mainly related to the composition and crystalline organization of the NP shell.

Moreover, regarding the electrochemical behavior of NP based aqueous colloidal dispersions Heyrovsky *et al*[16-20] have investigated polarography and voltammetry of nanosized particles. The results have shown that the particle and size distribution plays a very important role on the electrochemical properties of these materials. It yields different diffusion coefficients, different Faradaic charge, and an asymmetry on the reduction/oxidation peak potential.

---

[a] *Laboratório 3NANO, Instituto de Física, Universidade de Brasília, UnB, 70919-970 Brasília, Brazil*
[b] *Laboratório de Nanociência Ambiental e Aplicada-LNAA, Faculdade UnB Planaltina, UnB 73345-010 Brasília, Brazil.*
[c] *Sorbonne Universités, UPMC Univ. Paris 06, CNRS, Laboratoire PHENIX, Case 51, 4 place Jussieu, F 75005 Paris, France*
E-mail: relex@unb.br

See DOI: 10.1039/x0xx00000x

Previous research studies with magnetic NPs[21,22] reported voltammetric reduction of basic and citrated maghemite nanoparticles on mercury working electrode. The authors have shown that metallic iron is formed by the electrochemical reduction and that this iron interacts with the mercury electrode due to its wetting properties, leading to conductive magnetic fluids. They also determined the iron reduction potentials that lie between -0.4 to -1.2 V *vs.* SCE (Saturated Calomel Electrode) for Fe^{3+}/Fe^{2+} and between -1.5 to -1.8 V *vs.* SCE for Fe^{2+}/Fe^{0} depending on the nature of supporting electrolyte.

Furthermore, a recent review presents some nanoparticle voltammetry techniques, where systems in which the NPs mediate an electrochemical process are discussed.[23] As an example, the stripping voltammetry, which considers the direct oxidation or reduction of the nanoparticles, has shown that, for metallic NPs, the peak potential varies with the amount of electroactive material on the electrode surface.[24] Moreover, for Ag NPs of two different sizes supported on a carbon-fiber microelectrode with two different coverages, the peak potential of anodic stripping varies with both the NPs size and the total surface coverage. The authors enlighten that these features are consisted with a change in the thermodynamics of the NPs due to the influence of the altered surface energy.[25] Conversely the partial oxidation or reduction have been reported in such experiments, a problem that the authors overcame by applying a nano-impact technique.[26] Recent investigations, by using nano-impacts have been presented as a method of sizing metal oxide NPs.[27] The authors evaluated the impact of suspended Fe_3O_4 NPs against a solid working electrode surface during an anodic or cathodic controlled potential coulometry. Depending on the used potential, the whole NP structure is oxidized or reduced, thus yielding small faradaic charges, which can be related to the mean size of particles.

In this context, the main goal of the present work is to study the electrochemical behavior of pure maghemite and heterogeneous core-shell magnetic NPs by electroanalytical methods performed on acidic and neutral FFs. Square-wave voltammetry (SWV) was applied in order to investigate the surface reactivity as well as the influence of the NPs' composition on diluted cobalt, manganese, copper, zinc and maghemite ferrite based FFs. Afterwards, bulk electrolysis on maghemite and on cobalt ferrite FF based were performed using a mercury pool working electrode of a homemade electrolysis cell. The results are discussed in terms of a core-shell analysis in which the slightly different local structure of each phase is accounted.

Experimental Section

Reagents

The following pro analyse (P.A.) grade reagents, supplied from Vetec Química Fina, were used for NPs elaboration: $FeCl_3\cdot 6H_2O$ (purity 99%), $Fe(NO_3)_3\cdot 9H_2O$ (purity 99%), $(NH_4)_2Fe(SO_4)_2\cdot 6H_2O$ (purity 99%), $Co(NO_3)_2\cdot 6H_2O$ (purity 98%), $MnCl_2\cdot 4H_2O$ (purity 98%), $CuCl_2\cdot 2H_2O$ (purity 98%), $ZnCl_2\cdot H_2O$ (purity 99%), $C_6H_5Na_3O_7\cdot 2H_2O$ (purity 99%), NaOH (purity 99%), $(CH_3)_4NOH$ (25% in water) and HNO_3 (63% in water). The aqueous solutions were prepared with deionized water Type I (Millipore Milli-Q. Gradient quality).

Synthesis of electrostatically stabilized aqueous ferrofluids

The aqueous ferrofluids were prepared by following a well-known synthesis method, which has been described elsewhere.[28-30] The first step corresponds to the hydrothermal alkaline coprecipitation of ferrite nanoparticles. In this stage the size and the nanoparticle composition can be tuned by changing the hydroxide concentration of the synthesis medium or the chemical nature of the divalent metal.[30, 31] Maghemite NPs were obtained at room temperature where acidic stoichiometric mixture of $FeCl_2$ and $FeCl_3$ are alkalinized in order to precipitate magnetite (Fe_3O_4) NPs. Subsequently, the oxidation of Fe_3O_4 was performed by a hydrothermal treatment with $Fe(NO_3)_3$ 0.5 mol L^{-1} solution at 100 °C, yielding γ-Fe_2O_3 NPs. Core-shell ferrites NPs were also obtained through the coprecipitation method by alkalinizing 1:2 mixtures of M^{2+} and Fe^{3+} salts at 100 °C, where $M^{2+} = Co^{2+}$, Mn^{2+}, Cu^{2+} or Zn^{2+}.[6, 9, 28, 29, 32-35] Right after the coprecipitation step, the synthesized MFe_2O_4 nanoparticles are chemically stable with time, but if we disperse them in aqueous acid medium they tend to slowly dissolve and the ferrofluids are no longer viable.

Then, a hydrothermal treatment with iron (III) nitrate ($Fe(NO_3)_3$) at 100 °C is performed, as firstly proposed by Tourinho *et al*[28], in order to ensure the long term stability of the NPs in acidic medium. This protective treatment leads to the formation of the core-shell NPs structure and it has been described in detail elsewhere.[7] The model, which accounts for core-shell NPs based on different ferrite cores, has been tested by chemical and magnetic measurements performed at the various steps of the synthesis. More recently, X-ray absorption spectroscopy measurements performed on core shell NPs based on $ZnFe_2O_4$ core, have shown that undercoordinated divalent (zinc) cations are removed from the surface layer after the surface treatment[8]. A reduction of the coordination of iron ions is also observed since they are mainly located onto the NPs surface. The improvement of the NPs thermodynamical stability in acidic medium is a puzzling question. However, it can be observed that the ionic radius of M^{2+} is always larger than that of Fe^{3+} and thus Fe^{3+}–O bonds will be shorter and stronger than M^{2+}–O ones.[36] Then, because the acid dissolution of iron oxide involves the breakdown of both kind of bonds, replacing divalent metal by Fe^{3+} cations would protect the NPs surface. In the future it would be interesting to perform X-rays photoelectron spectroscopy (XPS) measurements as in ref. [37] since it is a highly surface specific technique, able to characterize the electronic state of each constituting atom of these materials.

In the final step of the ferrofluid synthesis, the NPs were conveniently peptized in aqueous acid medium by pH and ionic strength adjustments using HNO_3 solution. This procedure ensures an electrostatic repulsion between the NPs that is a consequence of a surface charge equilibrium, which leads to an electric double-layer formation.[15, 38] As a matter of fact, NPs surface behave as a diprotic Brönsted acid, and present a globally positive charge in acidic medium and a globally negative charge in basic medium. At the point of zero charge (PZC), which is close to 7 for these type of NPs, the overall surface charge is zero.[15, 38] Here we have prepared acid FFs at pH = 3 with different compositions, namely maghemite (γ-Fe_2O_3-NP) and core-shell NPs: $CoFe_2O_4@\gamma$–Fe_2O_3 (Co-NP), $MnFe_2O_4@\gamma$–Fe_2O_3 (Mn-NP), $CuFe_2O_4@\gamma$–Fe_2O_3 (Cu-NP) and $ZnFe_2O_4@\gamma$–Fe_2O_3 (Zn-NP).

We have also prepared FFs stable at pH = 7 based on $CoFe_2O_4@\gamma$–Fe_2O_3 NPs. The NPs surfaces were coated with citrate ligand by applying the method described in ref. [39,40]. A mass of sodium citrate ($C_6H_5Na_3O_7{\cdot}2H_2O$) was added in such a way that the molar ratio citrate to iron is 1:10 and the reaction was maintained for 30 minutes at 100 °C. After washing steps, at room temperature, in order to remove undesirable ions and reduce the ionic strength, the pH was controlled to 7 by adding drops of concentrated TMAOH, resulting in a stable citrate coated FF (Co-NP-Cit). The colloidal stability is ensured by the steric and electrostatic repulsive barrier of the ionized layer of citrate coating on NPs[41]. Besides citrate, other stabilizers have been used in the preparation of aqueous FFs as humic acid[41], sodium tartrate[42], poly(vinlypyrrolidone), trisodium citrate and maleic anhydride.[43]

X-Ray powder diffraction (XRD), TEM and HRTEM

The crystalline structure and the mean size of the synthetized NPs were evaluated from X-ray diffraction measurements on powder samples, obtained after the evaporation of the carrier liquids of FFs. These measurements have been performed at the Institute of Chemistry of University of Brasília (Brazil). An X-ray diffractometer D8 Focus from Bruker was operated at 40 kV/30 mA with Cu-Kα radiation (λ = 0.1541 nm) selected by a Ge 111 monochromator. The XRD patterns were obtained typically within $20° < 2\theta < 80°$ interval, with 0.05° step and 0.1° min^{-1} scan rate. Morphology and size distribution were investigated by Transmission Electron Microscopy (TEM, HRTEM), the pictures are obtained with a JEOL JEM- 2100 microscope under an accelerating voltage of 200 kV. These measurements have been performed at the Institute of Physics of University de Goiânia (Brazil).

Flame atomic absorption spectroscopy (FAAS) and chemical core-shell model

Samples compositions as well the amount of particles in solution were derived from the determination of metal ions in digested FF. Flame atomic absorption (FAAS) measurements were made on a Buck Scientific 200A spectrometer in solutions prepared from the FFs digested in hydrochloridric acid and diluted with deionized water.

In order to determine the volume fraction of NPs (ϕ_{NP}) into the FFs, a chemical core-shell model was introduced in ref. [7]. For pure maghemite sample (γ-Fe_2O_3-NP) the ϕ_{NP} are determined directly from [Fe]. However for all others synthesized NPs, that can be described as a core of stoichiometric ferrite surrounded by a shell of maghemite γ-Fe_2O_3, the volume ratio ϕ_{shell}/ϕ_{NP} can be calculated from the molar fraction $X_M = [M^{2+}]/([M^{2+}]+[Fe])$ and allow us to determine the shell thickness t_{sh}.

Square-wave voltammetry (SWV)

We performed voltammetric measurements using standard cells C3 and CGME from BASi, remotely controlled from a CV-50W potentiostat, with operation mode selected on Square-Wave Voltammetry (SWV). We have applied the SWV technique due to its reduced scan time, increased signal-to-noise ratio and higher accuracy and sensitivity compared to the Normal Pulse Voltammetry and Differential Pulse Voltammetry. In order to characterize and compare the electrochemical behaviour of iron in different systems, a study of iron (III) to iron (II) reduction was made with ionic solutions of iron (III) nitrate ($Fe(NO_3)_3$) and iron(III) citrate (Fe^{3+}–Cit), using HNO_3 10^{-3} mol L^{-1} and Na_3Cit 10^{-3} mol L^{-1} as supporting electrolyte, respectively. We performed these experiments with a glassy carbon working electrode (GCE) and an Ag/AgCl/NaCl 3M electrode as reference (0.209 V *vs.* SHE – Standard Hydrogen Electrode). All the samples were purged nitrogen flux for 10 minutes. In the case of acid FFs we used these same experimental conditions. For the citrated FF sample we used Na_3Cit 10^{-3} mol L^{-1} as supporting electrolyte and the pH was maintained around 7. We performed the measurement using a hanging mercury drop electrode (HMDE) as working electrode to account for the shift of the reduction peak expected in functionalized FFs.

Table 1. Experimental results arising from physicochemical analysis of the samples investigated. d_{XRD} is the XRD mean diameter. ϕ_{NP} is the volume fraction of FFs. ϕ_{shell}/ϕ_{NP} is the ratio of the volume fraction of maghemite shell to the total volume in heterogeneous core-shell NPs, t_{sh} is the thickness of the superficial layer.

Sample	d_{XRD} (nm)	d_{TEM} (nm)	σ_{TEM}	ϕ_{NP} (%)	ϕ_{shell}/ϕ_{NP}	t_{sh} (nm)
Co-NP	12.9	10.7	0.25	8.5	0.25	0.66
Mn-NP	9.1	11.2	0.29	10.4	0.27	0.53
Cu-NP	7.6	6.3	0.24	5.9	0.65	1.21
Zn-NP	7.3	6.6	0.24	6.2	0.45	0.72
γ-Fe_2O_3-NP	8.2	6.8	0.24	8.3	-	-

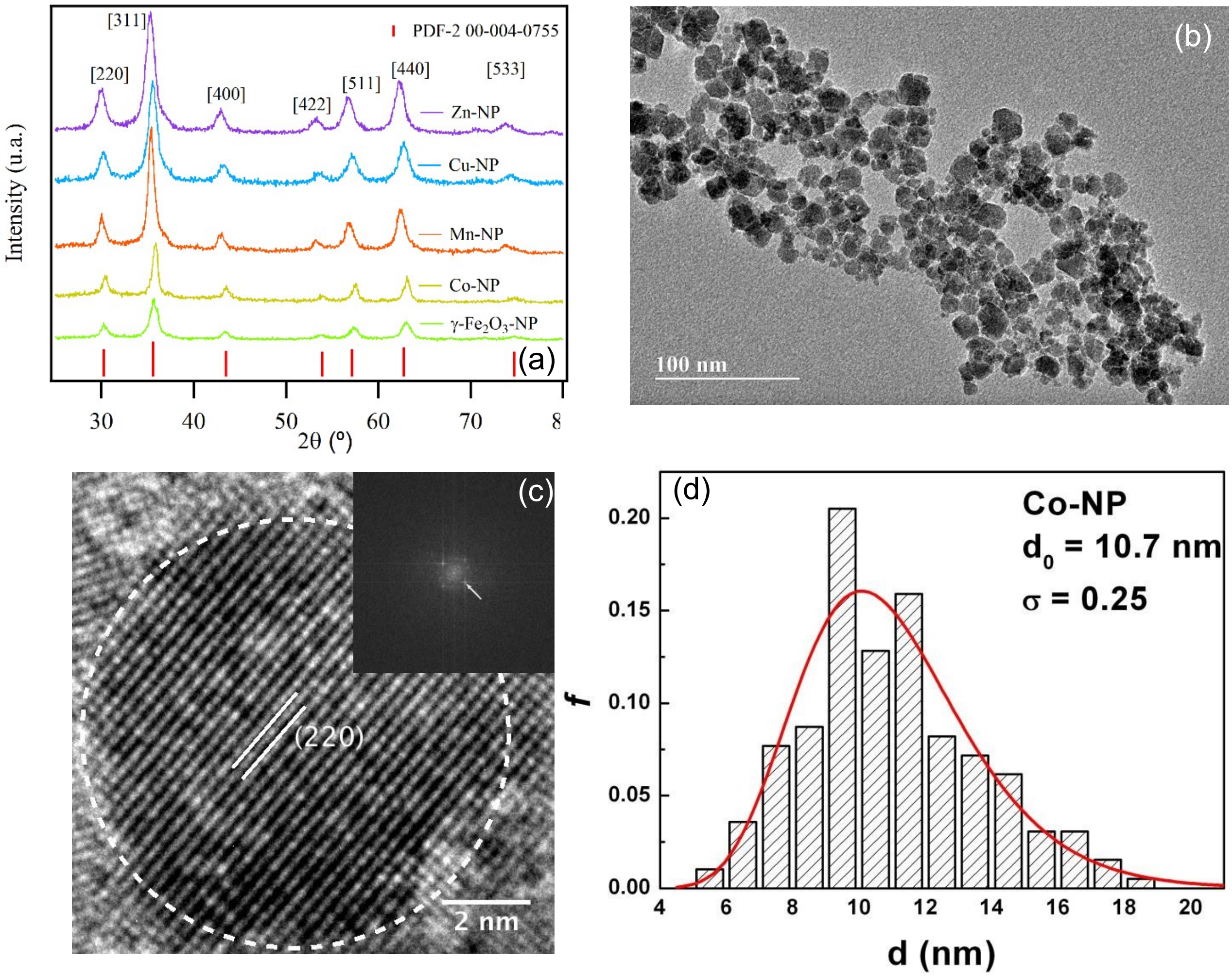

Figure 1. (a) X-ray powder diffraction patterns of core-shell maghemite, Co-, Mn-, Cu- and Zn- ferrites based NPs. The interplanar spacing positions for cubic spinel crystalline structure were extracted from PDF-2: 00-004-0755. (b, c): Typical TEM (b) and high-resolution HRTEM (c) images of core-shell ferrite NPs for sample Co-NP. (d) is the normalized histogram of the NP size distribution deduced from transmission electron microscopy (TEM) measurements together with its corresponding Fourier Transform.

Bulk electrolysis: controlled potential coulometry

We performed controlled potential coulometry electrolysis measurements using a homemade bulk electrolysis cell remotely controlled with a CV-50W potentiostat. The experiments were realized using a mercury pool working electrode with a large surface area in order to enhance the rate of electrolysis. In each measurement, a small volume of mercury was placed inside a cylindrical shaped cell of 3.5 cm of diameter and with a platinum contact at the bottom. A magnetic bar was used to constantly stir the solutions and renew the mercury surface during the electrolysis. The platinum coil auxiliary electrode was isolated from the analyte solutions with a glass tube that has a porous ceramic frit. For all measurements, we used 5 mL of HNO_3 10^{-3} mol L^{-1} as supporting electrolyte, which was systematically purged with nitrogen flux for 10 minutes and then electrolyzed in order to subtract its current effect. The bulk electrolysis potential was chosen according to the SWV results of the FF samples. Then 10 μL of each FF sample was added to the electrolysis cell corresponding to final volume fraction of around 0.02%. The measurements were carried out under constant stirring and slight nitrogen flow until the complete stabilization of the current.

Results and discussion

Structural characterization and mean diameter determination – XRD and TEM/HRTEM

Fig. 1a presents the diffractograms of all the samples investigated here, the spinel structure (Fd3m space group) is confirmed. The average lattice parameters are calculated from the six most intense lines [220], [311], [400], [422], [511], [440] and [533], analysed through the well-known Bragg's law. These results are in good agreement with the International Centre for Diffraction Data (ICCD) patterns for spinel ferrites. Nanocrystals sizes were evaluated by Scherrer's formula[44]

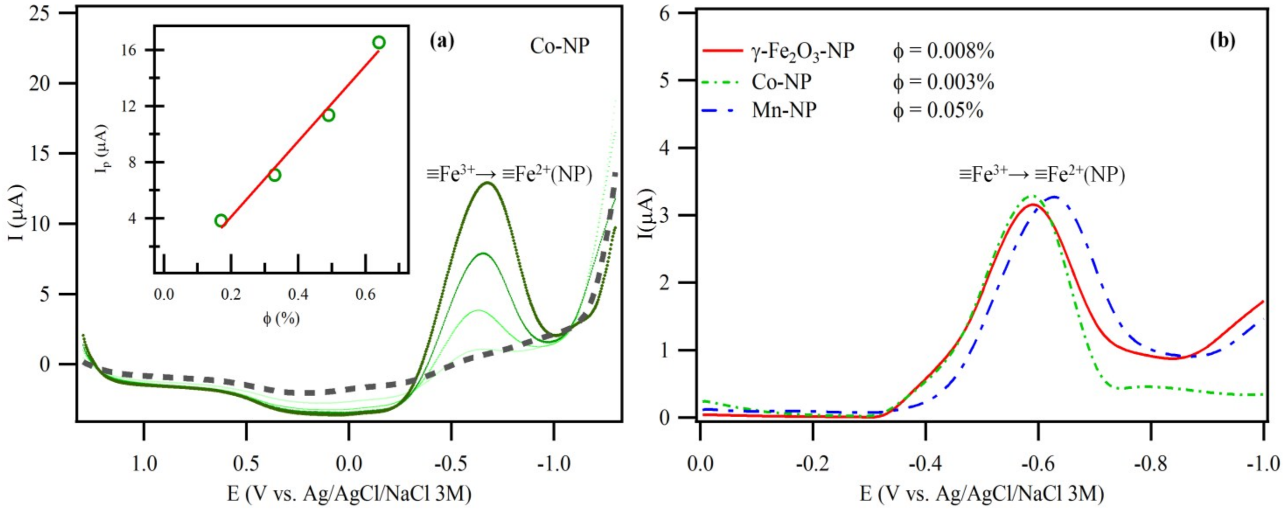

Figure 2. (a) Square-wave voltammograms performed on a glassy carbon electrode (GCE) with cobalt ferrite NPs. The dashed line corresponds to the supporting electrolyte $[HNO_3] = 10^{-3}$ mol L^{-1}, the green lines to the successive additions of Co-NP based FF; inset shows the linearity of peak currents in different volume fractions; (b) Comparison of the electrochemical behavior with reduction of superficial $\equiv Fe^{3+}$ in Co-NP, Mn-NP and γ-Fe_2O_3-NP (see text for details).

applied to the most intense [311] line. The determined mean diameters (d_{XRD}) are presented on Table 1.

Fig. 1b, displays a typical image of the NPs, here represented by Co-NP. The images of the particles indicate that they have most predominantly spherical shape.

Fig. 1c presents a typical high-resolution (HRTEM) image of a single nanoparticle for sample Co-NP together with its corresponding Fourier Transform. It enabled the observation of the (220) plane of the crystal lattice and that the NPs present good crystallinity. The lattice spacing can be directly measured from the image, and the projected symmetry is revealed by the Fourier transformation. It is then possible to determine the lattice plane spacing of the order of 2.9 Å that corresponds to the Miller indices (220) for both, cobalt ferrite and maghemite phases. It is indeed, in good agreement with the International Centre for Diffraction Data (ICCD) patterns for spinel ferrites. In order to evaluate size distribution of the NPs investigated here a histogram based on about 200-particle size is obtained for each sample.

Fig. 1d shows the histogram for sample Co-NP. The size distribution is well accounted for by a Log-normal law. Fitting of the histogram yields the median diameter ($d_0 = 10.7$ nm) and polydispersity ($\sigma = 0.25$) for sample Co-NP. The results of mean diameter (d_0) and size distribution (σ) for all the samples investigated here are listed on Table 1

Volume fraction of NPs and thickness of NPs shell

The concentration of metals (iron and bivalent ones), given in mol L^{-1}, into NPs can be expressed in terms of volume fraction (ϕ_{NP}, which relates the volume of the NPs with the volume of the dispersion) using the molar volume (V_M) of ferrites.[45] In the case of pure maghemite, the volume fraction is then given as $\phi_{NP} = [Fe](\text{mol } L^{-1}) V_M^{\gamma\text{-}Fe_2O_3}$, while in heterogeneous core-shell based FFs the volume fraction is expressed as the sum ($\phi_{NP} = \phi_{core} + \phi_{shell}$) the volume fractions of the central ferrite, $\phi_{core} = [M] V_M^{MFe_2O_4}$ and of the surface, $\phi_{shell} = [Fe] V_M^{\gamma\text{-}Fe_2O_3} = 0.5([Fe]-2[M])\ V_M^{\gamma\text{-}Fe_2O_3}$.[7] The obtained values of the volume fractions and of the thickness of NPs shell are summarized in Table 1

Table 2. Peak potentials (E_p) for all samples investigated in this work compared to the values obtained for iron (III) nitrate ($Fe(NO_3)_3$) and iron(III) citrate (Fe^{3+}–Cit).

Sample	Supporting Electrolyte	Working Electrode	Half-Reaction	E_p (V *vs.* Ag/AgCl/NaCl 3M)
$Fe(NO_3)_3$	HNO_3 pH = 3	GCE	$Fe^{3+} + e^- \rightarrow Fe^{2+}$	+0.49
Fe^{3+}-citrate	HNO_3 pH = 3	GCE	Fe^{3+}-Cit$+ e^- \rightarrow Fe^{2+}$-Cit	+0.16
Co-NP	HNO_3 pH = 3	GCE	$\equiv Fe^{3+} + e^- \rightarrow \equiv Fe^{2+}$	-0.59
Mn-NP	HNO_3 pH = 3	GCE	$\equiv Fe^{3+} + e^- \rightarrow \equiv Fe^{2+}$	-0.63
Cu-NP	HNO_3 pH = 3	GCE	$\equiv Fe^{3+} + e^- \rightarrow \equiv Fe^{2+}$	-0.64
Zn-NP	HNO_3 pH = 3	GCE	$\equiv Fe^{3+} + e^- \rightarrow \equiv Fe^{2+}$	-0.65
γ-Fe_2O_3-NP	HNO_3 pH = 3	GCE	$\equiv Fe^{3+} + e^- \rightarrow \equiv Fe^{2+}$	-0.60
Co-NP-Cit	Na_3Cit 1mM pH = 7	HDME	$\equiv Fe^{3+} + e^- \rightarrow \equiv Fe^{2+}$	-0.68
			$\equiv Fe^{3+}$-Cit$+ e^- \rightarrow \equiv Fe^{2+}$–Cit	-1.21
			$\equiv Fe^{2+} + 2\ e^- \rightarrow \equiv Fe$	-1.38

Analysis of the square-wave voltammetry curves

As described in the experimental section, the SWV method has been applied for Fe^{3+} and Fe^{3+}–Cit ionic solutions and we evaluated the reduction peaks as +0.49 V and +0.16 V (*vs.* Ag/AgCl/NaCl 3M) for the pairs Fe^{3+}/Fe^{2+} and Fe^{3+}/Fe^{2+}–Cit, respectively. These results indicate that it is more difficult to reduce iron in the complex Fe^{3+}–Cit that in free Fe^{3+}. We describe in the following the results obtained for FF samples using the same experimental parameters values, which have been fixed by the standard procedure.

The voltammograms presented in Fig. 2a show that the core-shell $CoFe_2O_4@\gamma\text{-}Fe_2O_3$ ferrite nanoparticles are electroactive. The reduction peak located at a cathodic potential equal to -0.59 V (*vs.* Ag/AgCl/NaCl 3M) corresponds to the one observed at -0.86 V (*vs.* Ag/AgCl/KCl_{sat}) in ref. [46] and the cathodic current is attributed to the reduction of the iron (III) of the nanocrystal according to the reaction:

$$3\,\gamma\text{-Fe}_2\text{O}_3 + 2\,\text{H}^+ + 2\,\text{e}^- \rightarrow 2\,\text{Fe}_3\text{O}_4 + \text{H}_2\text{O}\,. \qquad (1)$$

The variations between the values of the reduction potential found here and in ref. [46] are due to differences in the experimental conditions of each voltammetric measurement (working and reference electrodes, pH and supporting electrolyte). When compared to the free iron reduction, the value of -0.59 V corresponds to a large shift of the order of 1 V. It shows that the reduction of iron (III) is also more difficult in the nanocrystal lattice than in true solutions. This is due to the basic difference of electron transfer process in these two systems.[20] In the electroreduction of NP, electrons from the electrode are transferred to the electron conduction band of the semiconducting NP whereas in the electroreduction of free ions the electrons are transferred to atomic orbitals. Thus, the comparison of the three systems, Fe^{3+}, Fe^{3+}–Cit ionic solutions and our NPs dispersions, shows that the peak potential of iron reduction is shifted towards more cathodic electrochemical region, due to iron (III) decreasing oxidizing strength, as predicted by the Nernst formalism,[47] when the environment goes from true solutions to coordinated configurations.

Moreover, no contribution is observed around +0.49 V (*vs.* Ag/AgCl) demonstrating that FF dispersions do not contain any free iron ions. The inset of Fig. 2a exhibits the current intensity measured as a function of NP volume fraction. It clearly indicates that the magnitude of the peaks is directly proportional to the NP concentration showing therefore that the cathodic current originates from the NP.

Fig. 2b presents the voltammograms of $\gamma\text{-}Fe_2O_3$-NP, Co-NP and Mn-NP samples. The peak potentials are very close to the same value, around -0.6 V (*vs.* Ag/AgCl). In the case of Cu-NP and Zn-NP samples, not shown here, the reduction peak is also encountered at the same position, as presented in Table 2, which lists the peak potentials for all samples investigated in this work compared to the values obtained for both iron (III) solutions. The slight shift of the peak for Mn-NP is related to the increased polydispersity of this sample, as observed for other nanoparticles.[48-50] These results demonstrate that the NP peak potential is very weakly affected by the chemical composition of the core indicating that the reduction phenomena occur at the surface of the NP. It is clearly a property that reflects the crystalline organization of the particle shell. As in all our NPs the surface layer is the same, made of $\gamma\text{-}Fe_2O_3$, the surface iron (III) ions will present similar oxidizing strength. Additionally, although the characteristic size of all investigated NPs samples are different (see Table 1) it does not seem to affect the NPs electroactivity, which here would be more related to the similar surface of the core-shell NPs. However, more experiments performed on samples with lower polydispersity would better enlighten this question.

Fig. 3 exhibits the voltammograms of Co-NP-Cit sample

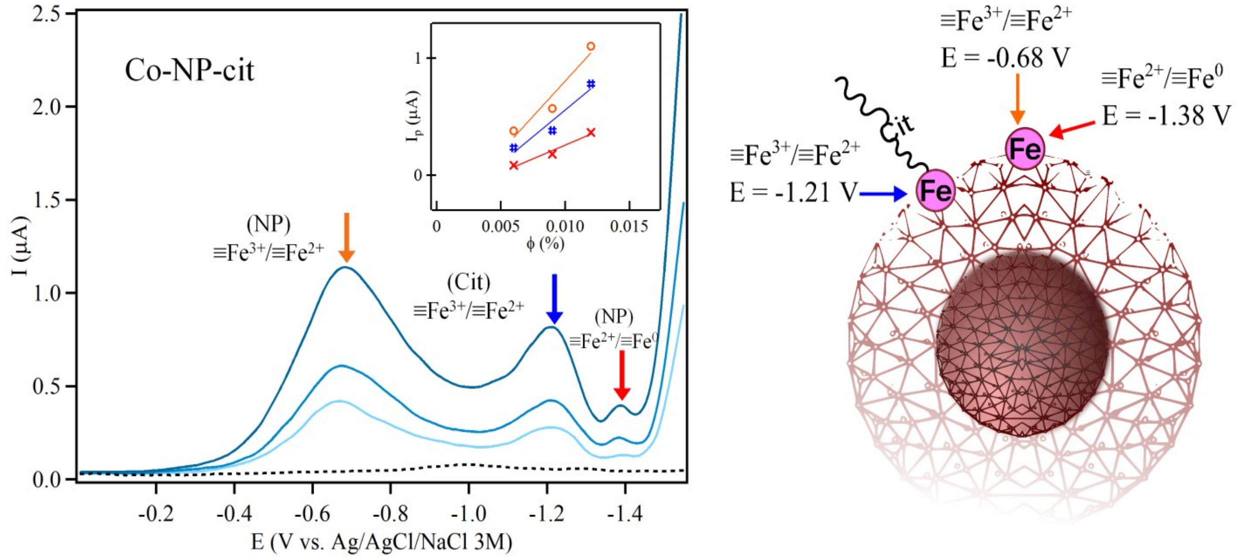

Figure 3. Square-wave voltammograms of Co-NP-Cit sample for three volume fraction of NPs. The inset displays the peak current (*Ip*) as a function of ϕ_{NP}. On the right side, schematic representation of the NPs surface reduction for the same sample.

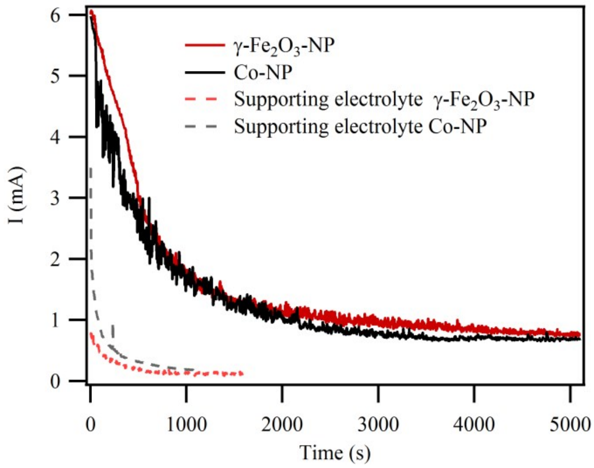

Figure 4. Curves current-time obtained by the electrolysis of diluted acid FFs (ϕ = 0.02%) through controlled potential coulometry performed on a mercury pool working electrode and supporting electrolyte [HNO_3] = 10^{-3} mol L^{-1}. Red line corresponds to the γ-Fe_2O_3-NP and black line to the Co-NP.

obtained for three volume fractions of NPs. All present two well-defined reduction peaks. Regarding the experimental conditions of measurements (pH, supporting electrolyte and working electrode), we consider here that the first peak, located at -0.68 V (*vs.* Ag/AgCl), is associated to the reduction of NPs iron (III). We also assume that the second one, at a more cathodic potential around -1.21 V (*vs.* Ag/AgCl), is related to the citrated iron (III) sites of the NPs, since ligands in coordinative bond transfer electron density to the metal ion, shifting the electrode potential to lower values. It therefore means a coexistence of non-citrated and citrated metallic sites onto the NPs surface. Then, the peak located at -1.38 V (*vs.* Ag/AgCl), of lower intensity, would be related to the Fe^{2+}/Fe^0 redox couple, as predicted by previous determinations in similar FF system.[22, 46] In ref. [22], the authors attribute the observed peaks of their voltammograms, in the region -0.4 to -1.2 V (*vs.* SCE), to a partial reduction of the maghemite NPs leading to a release of iron (II) ions into the bulk solution. It was not observed in our case, since probably the pH and supporting electrolyte of our experiments are different from those of ref. [22] and would change the kinetics of the NPs dissolution and iron (II) release. Moreover, in our measurements, as in ref. [22], the peak current is proportional to the volume fraction of NPs as exhibited in the inset of Fig. 3. This result indicates that the reduction peaks observed here more correspond to electroactive species from the NPs surface.

Electron diffusion at the NP/electrode interface

In this experiment, the purpose is to investigate the electrolysis of iron (III) in spinel ferrite NPs at controlled potential (Controlled Potential Coulometry). The potential value has been chosen equal to -0.95 V (*vs.* Ag/AgCl), more cathodic than that of the voltammetric reduction peak of ferrites NPs, in order to take into account the overvoltage and to ensure bulk electrolysis conditions. During the measurement, a whitening of the solutions occurs, from reddish or blackish to almost transparent, for γ-Fe_2O_3-NP and Co-NP samples, respectively. However, no visual modifications seem to appear at the mercury electrode.

Fig. 4 presents the decay time of the current intensity *I*, corresponding to electron diffusion at the NP/electrode interface. At the end of the electrolysis, which occurs after about 1 hour, the integration of *I vs. t* curve leads to the net charge Q_T involved in the reduction of NPs iron (III). According to Faraday's Law,

$$Q_T = \int I dt = zFn\,, \qquad (2)$$

where *F* is the Faraday constant (*F* = 96485 C mol^{-1}). In our case, *z* = 1 to account for the number of exchanged electrons in the reduction of NPs iron (III) and *n* is its number of moles. The total net charges Q_T deduced from integration are 2.105 and 3.209 coulombs for γ-Fe_2O_3-NP and Co-NP samples, respectively. Then we determined in each case the moles number of reduced iron $n_{Fe^{2+}}$ using Eq. (2) and the values are listed in Table 3. Both are lower than the values of the moles number of total iron n_{Fe}^{total} determined from FAAS measurements. One can therefore conclude that only a fraction of iron (III) present in the NPs was reduced at the NP/electrode interface leading to the formation of hybrid nanoparticles composed by a ferrite core and a shell of electrolyzed material.

We will take into account this result in a model that considers that the electrochemical reduction homogeneously occurs in a surface layer of each individual NPs. Indeed, during the cathodic controlled potential coulometry, all individually dispersed NPs are at contact with the Hg electrode surface, inducing redox process over a fraction of each NP structure. Then, as in ref. [27], the individual net charge Q_P can be correlated to the volume that contains all the reduced iron. We thus calculate here the volume V_{el} of the surface layer associated to the partial electrolysis of a single spherical particle and its thickness t_{el} as:

$$V_{el} = V_{NP} - (n_{Fe}^{total} - n_{Fe^{2+}})\frac{V_M}{2} \approx \frac{4}{3}\pi r^3\left[1-\left(\frac{r-t_{el}}{r}\right)^3\right], \qquad (3)$$

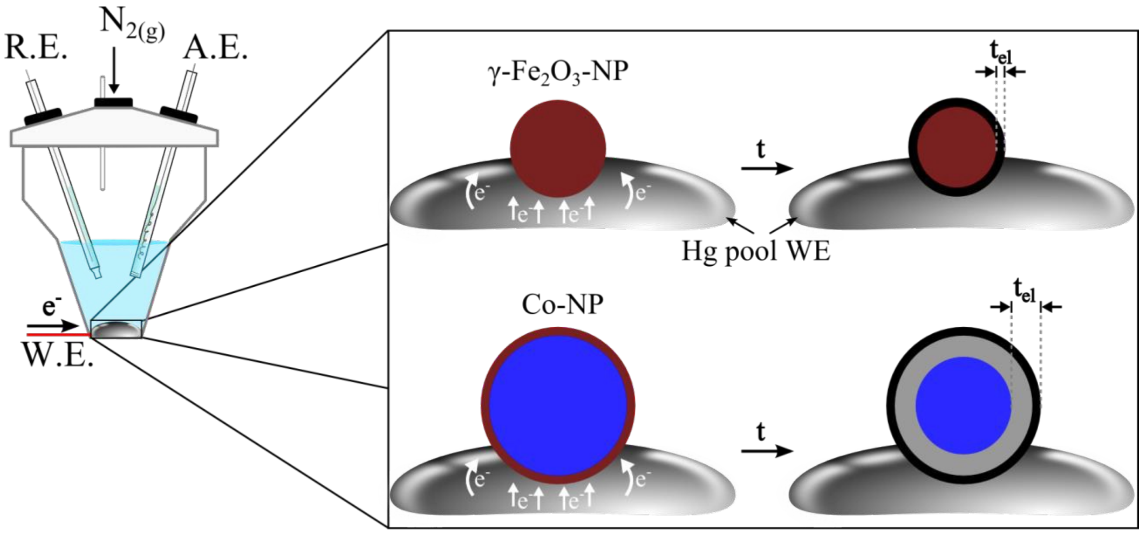

Figure 5. Schematic representation of the controlled potential coulometry device and the model for the composition of the electrolyzed ferrites NPs. An Ag/AgCl/NaCl 3M electrode was used as reference (R.E.) and a platinum coil as auxiliary electrode (A.E.). The measurements were carried out under constant stirring and slight nitrogen flow until the complete stabilization of the current. The electrolysis process occurs on the surface of a mercury pool working electrode (W.E.) only over a fraction of each NP structure, which produces hybrid nanoparticles composed by a ferrite core and a shell of electrolyzed material with a t_{el} thickness. For the γ-Fe_2O_3-NP sample, the electrolyzed shell corresponds to magnetite (black) while for the Co-NP sample the shell consists of two phases: an outer one of magnetite and an intermediary layer (gray) wherein all iron cations are in the Fe^{2+} state.

where r is the radius of the NPs and V_M is the molar volume of the non-reduced fraction of the NP material. Using the radius values determined from XRD measurements, the molar volume of maghemite or cobalt ferrite equals to 32.86 $cm^3\ mol^{-1}$ and 44.67 $cm^3\ mol^{-1}$, respectively, and one can deduce the fraction of the electrolyzed shell and its thickness listed in Table 3.

Our model equally considers the reduction of iron in both types of spinel sites, tetrahedral and octahedral ones. Only 41% of the whole volume of γ-Fe_2O_3-NP (radius 4.1 nm) is reduced, a value that corresponds to a thickness associated to the partial electrolysis of the NPs of 0.7 nm. This is of the order of magnitude of the maghemite lattice cell (a = 0.833 nm). On the other hand, the larger Co-NP (radius 6.5 nm) have 76% of its volume reduced using the same conditions (working electrode, supporting electrolyte and pH) leading to a thickness of 2.4 nm.

This larger value when compared to maghemite NPs can be enlightened by considering that the number of iron ions per cubic cell is smaller in cobalt ferrite when compared to maghemite. Then, the volume fraction of the shell containing the reduced iron ions should be expected to be larger in core-shell NPs based on cobalt ferrite than in homogeneous maghemite NPs.

Fig. 5 exhibits the schematic representation of the controlled potential coulometry device and the model for the composition of the electrolyzed ferrites NPs. In the case of the γ-Fe_2O_3-NP sample, the formed hybrid nanoparticles are composed by a maghemite core surrounded by a shell of magnetite, according to the redox reaction described in equation (1). For the Co-NP sample, the magnetic nanohybrids present a cobalt ferrite core and a shell of electrolyzed material which consists of two phases: an outer one of magnetite and an intermediary layer wherein all the iron cations are in the Fe^{2+} state. In this phase, the stabilization of the divalent iron cations into the spinel lattice induces deviation from stoichiometry and creation of vacancies to account for electroneutrality.

The electrochemically assisted elaboration of hybrid magnetic nanoparticles has been very recently reported by Wang *et al.* [51] The authors have used a sequenced in-situ redox of metal ions and/or precipitation of metal oxides to obtain varieties of gradient core-shell nanohybrids composed by CoM, FeM, AuM, AgM (M = Zn or Al) alloys as cores and transition metal gradient-doping ZnO or Al_2O_3 as shells. This new synthesis strategy has endowed the nanoparticles with unique magnetic and optical properties. In such a context, we intend to perform further experiments under closely controlled conditions in order to not only monitor our magnetic nanohybrids

Table 3. Characteristics of electrolyzed ferrites NPs (nanohybrids). n_{Fe}^{total} corresponds to the total amount of iron added to the electrolysis cell, n_{Fe}^{2+} is the total amount of reduced iron, $V_{el.}/V_{NP}$ is the ratio of reduced NP per its total volume and $t_{el.}$ is the thickness of an electrochemical reduced shell.

Sample	n_{Fe}^{total} (μmol)	n_{Fe}^{2+} (μmol)	V_{el}/V_{NP}	t_{el} (nm)
γ-Fe_2O_3-NP	52	22	0.41	0.7
Co-NP	43	33	0.76	2.4

elaboration, but also investigate their physicochemical behaviour and accurate chemical composition.

Conclusions

In this work, we have investigated the electrochemical reduction of iron (III) in a series of maghemite and core-shell ferrites NPs of ferrofluids dispersions. Each NPs sample presents different chemical composition of the core as well as different median sizes and polydispersity. These ferrite NPs are electroactive and their voltammograms present a reduction peak that lies, for all samples, at a cathodic potential between -0.59 V and -0.65 V (*vs.* Ag/AgCl/NaCl 3M). It is attributed to the reduction of iron (III) of the NPs surface since the intensity of the peak is proportional to the particles volume fraction and completely vanishes after addition of salt and consequent NPs coagulation. Neither the chemical composition of the core, nor the size distribution (mean size and polydispersity) seems to have a significant influence on the peak location. When compared to the reduction peak of free iron in ionic solutions, the NPs reduction peak of magnetic colloids is shifted about 1 V. This expected result manifests the different electron transfer process in each system and shows that iron (III) oxidizing strength decreases when iron environment goes from ion solutions to coordinated configurations. When the nanoparticles surface is coated by citrate ligands, the obtained voltammograms indicate a coexistence of non-citrated and citrated metallic sites onto the NPs surface.

We also investigate the electrolysis of iron (III) in maghemite NPs and core-shell NPs based on cobalt ferrite at a controlled potential (-0.95 V (*vs.* Ag/AgCl)) in order to ensure bulk electrolysis conditions. In each sample, only a fraction of the iron (III) contained in the NPs is reduced leading to the formation of a nanohybrid. We account for this result by considering that iron (III) reduction occurs, for each particle, only in a superficial layer. Then, the individual net charge deduced from the integration of current-time curves is correlated to the volume of this surface shell. For maghemite NPs, the thickness of the shell is about the cubic cell size of the spinel structure. For cobalt ferrite based NPs, the thickness is larger, which is probably related to the lower number of iron ions per cobalt ferrite cubic cell when compared to maghemite.

Further experiments, performed on less polydisperse samples, on core-shell NPs with variable maghemite shell and on different characteristics time will be of great importance in the next future along with the investigation of the physicochemical properties of the hybrid nanoparticles.

Acknowledgments

We acknowledge the CAIQ/UnB for XRD measurements. We also thank the exchange program CAPES-COFECUB n° 714/11, the Brazilian agencies CNPq and FAPDF. C. L. Filomeno is very grateful for the CAPES grant nº. 99999.001111/2014-00.

Dr. F. A. Tourinho is deceased during the redaction of this paper but, as an electrochemistry specialist, he was at the origin of this work. We dedicate this article to his memory.

References

1. K. Cho, X. Wang, S. Nie, Z. Chen and D. M. Shin, *Clinical Cancer Research*, 2008, **14**, 1310-1316.
2. I. Brigger, C. Dubernet and P. Couvreur, *Advanced Drug Delivery Reviews*, 2002, **54**, 631-651.
3. L. Asin, G. F. Goya, A. Tres and M. R. Ibarra, *Cell Death & Disease*, 2013, **4**.
4. C. Wilhelm, J.-P. Fortin and F. Gazeau, *Journal of Nanoscience and Nanotechnology*, 2007, **7**, 2933-2937.
5. F. G. Silva, R. Aquino, F. A. Tourinho, V. I. Stepanov, Y. L. Raikher, R. Perzynski and J. Depeyrot, *Journal of Physics D-Applied Physics*, 2013, **46**.
6. R. Cabreira-Gomes, F. G. Silva, R. Aquino, P. Bonville, F. A. Tourinho, R. Perzynski and J. Depeyrot, *Journal of Magnetism and Magnetic Materials*, 2014, **368**, 409-414.
7. J. A. Gomes, M. H. Sousa, F. A. Tourinho, R. Aquino, G. J. da Silva, J. Depeyrot, E. Dubois and R. Perzynski, *Journal of Physical Chemistry C*, 2008, **112**, 6220-6227.
8. J. A. Gomes, G. M. Azevedo, J. Depeyrot, J. Mestnik, F. L. O. Paula, F. A. Tourinho and R. Perzynski, *Journal of Physical Chemistry C*, 2012, **116**, 24281-24291.
9. O. Bomati-Miguel, P. Tartaj, M. P. Morales, P. Bonville, U. Golla-Schindler, X. Q. Zhao and S. Veintemillas-Verdaguer, *Small*, 2006, **2**, 1476-1483.
10. C. Blanco-Andujar, D. Ortega, P. Southern, Q. A. Pankhurst and N. T. K. Thanh, *Nanoscale*, 2015, **7**, 1768-1775.
11. P. B. Shete, R. M. Patil, R. S. Ningthoujam, S. J. Ghosh and S. H. Pawar, *New Journal of Chemistry*, 2013, **37**, 3784-3792.
12. A. Makridis, K. Topouridou, M. Tziomaki, D. Sakellari, K. Simeonidis, M. Angelakeris, M. P. Yavropoulou, J. G. Yovos and O. Kalogirou, *Journal of Materials Chemistry B*, 2014, **2**, 8390-8398.
13. L. Zhou, J. Yuan and Y. Wei, *Journal of Materials Chemistry*, 2011, **21**, 2823-2840.
14. J.-H. Lee, J.-t. Jang, J.-s. Choi, S. H. Moon, S.-h. Noh, J.-w. Kim, J.-G. Kim, I.-S. Kim, K. I. Park and J. Cheon, *Nature Nanotechnology*, 2011, **6**, 418-422.
15. A. F. C. Campos, R. Aquino, F. A. Tourinho, F. L. O. Paula and J. Depeyrot, *European Physical Journal E*, 2013, **36**.
16. K. Micka, *Collection of Czechoslovak Chemical Communications*, 1965, **30**, 223-&.
17. M. Heyrovsky, J. Jirkovsky and B. R. Muller, *Langmuir*, 1995, **11**, 4293-4299.
18. M. Heyrovsky, J. Jirkovsky and M. Struplovabartackova, *Langmuir*, 1995, **11**, 4300-4308.
19. M. Heyrovsky, J. Jirkovsky and M. Struplovabartackova, *Langmuir*, 1995, **11**, 4309-4312.
20. M. Heyrovsky and J. Jirkovsky, *Langmuir*, 1995, **11**, 4288-4292.

21. E. Dubois, J. Chevalet and R. Massart, *Journal of Molecular Liquids*, 1999, **83**, 243-254.
22. E. Dubois and J. Chevalet, *Langmuir*, 2003, **19**, 10892-10900.
23. C. Batchelor-McAuley, E. Kaetelhoen, E. O. Barnes, R. G. Compton, E. Laborda and A. Molina, *Chemistryopen*, 2015, **4**, 224-260.
24. H. S. Toh, C. Batchelor-McAuley, K. Tschulik, M. Uhlemann, A. Crossley and R. G. Compton, *Nanoscale*, 2013, **5**, 4884-4893.
25. C. C. M. Neumann, C. Batchelor-McAuley, K. Tschulik, H. S. Toh, P. Shumbula, J. Pillay, R. Tshikhudo and R. G. Compton, *Chemelectrochem*, 2014, **1**, 87-89.
26. N. V. Rees, Y.-G. Zhou and R. G. Compton, *Rsc Advances*, 2012, **2**, 379-384.
27. K. Tschulik, B. Haddou, D. Omanovic, N. V. Rees and R. G. Compton, *Nano Research*, 2013, **6**, 836-841.
28. F. A. Tourinho, R. Franck and R. Massart, *Journal of Materials Science*, 1990, **25**, 3249-3254.
29. R. Massart, *Ieee Transactions on Magnetics*, 1981, **17**, 1247-1248.
30. M. H. Sousa, F. A. Tourinho, J. Depeyrot, G. J. Silva and M. C. F. L. Lara, *Journal of Physical Chemistry B*, 2001, **105**, 1168-1175.
31. R. Aquino, F. A. Tourinho, R. Itri, M. Lara and J. Depeyrot, *Journal of Magnetism and Magnetic Materials*, 2002, **252**, 23-25.
32. F. Tourinho, R. Franck, R. Massart and R. Perzynski, *Trends in Colloid and Interface Science Iii*, 1989, **79**, 128-134.
33. A. Abou-Hassan, S. Neveu, V. Dupuis and V. Cabuil, *Rsc Advances*, 2012, **2**, 11263-11266.
34. V. Cabuil, V. Dupuis, D. Talbot and S. Neveu, *Journal of Magnetism and Magnetic Materials*, 2011, **323**, 1238-1241.
35. O. Horner, S. Neveu, S. de Montredon, J.-M. Siaugue and V. Cabuil, *Journal of Nanoparticle Research*, 2009, **11**, 1247-1250.
36. P. S. Sidhu, R. J. Gilkes, R. M. Cornell, A. M. Posner and J. P. Quirk, *Clays and Clay Minerals*, 1981, **29**, 269-276.
37. Y. J. Song, S. X. Ji, R. S. Li, J. Ding, X. M. Shen, R. M. Wang, R. W. Xu and X. Y. Gu, *Journal of Physical Chemistry C*, 2013, **117**, 17274-17284.
38. A. F. C. Campos, F. A. Tourinho, G. J. da Silva, M. Lara and J. Depeyrot, *European Physical Journal E*, 2001, **6**, 29-35.
39. M. Mamusa, J. Sirieix-Plenet, F. Cousin, R. Perzynski, E. Dubois and V. Peyre, *Journal of Physics-Condensed Matter*, 2014, **26**.
40. E. Dubois, V. Cabuil, F. Boue and R. Perzynski, *Journal of Chemical Physics*, 1999, **111**, 7147-7160.
41. A. Hajdu, E. Illes, E. Tombacz and I. Borbath, *Colloids and Surfaces a-Physicochemical and Engineering Aspects*, 2009, **347**, 104-108.
42. A. F. C. Campos, M. A. Ferreira, E. P. Marinho, F. A. Tourinho and J. Depeyrot, *Physics Procedia*, 2010, **9**, 45-48.
43. Y. J. Song, R. X. Wang, R. Rong, J. Ding, J. Liu, R. S. Li, Z. H. Liu, H. Li, X. Y. Wang, J. Zhang and J. Fang, *European Journal of Inorganic Chemistry*, 2011, 3303-3313.
44. C. Hammond, *The Basics of Crystallography and Diffraction*, Oxford University Press, New York, 3 edn., 1997.
45. B. M. Berkovski, *Magnetic Fluids and Applications Handbook*, Begell House Inc. Publ., New York, 1996.
46. G. V. M. Jacintho, P. Corio and J. C. Rubim, *Journal of Electroanalytical Chemistry*, 2007, **603**, 27-34.
47. D. A. Skoog, D. M. West, F. J. Holler and S. R. Crouch, *Fundamentals of Analytical Chemistry*, Thomson, Toronto, 8th edn., 2004.
48. P. Letellier and M. Turmine, *Electrochimica Acta*, 2014, **127**, 384-389.
49. H. Karami, B. Kafi and S. N. Mortazavi, *International Journal of Electrochemical Science*, 2009, **4**, 414-424.
50. K. Z. Brainina, L. G. Galperin, E. V. Vikulova and A. L. Galperin, *Journal of Solid State Electrochemistry*, 2013, **17**, 43-53.
51. R. M. Wang, W. T. Yang, Y. J. Song, X. M. Shen, J. M. Wang, X. D. Zhong and S. A. Li, *Scientific Reports*, 2015, **5**.

Table of Contents

The electroactivity of MFe_2O_4@γ-Fe_2O_3 (M = Mn, Co, Cu and Zn) nanoparticles occurs at the surface layer and reflects the surface environment.